Xenon Ion Implantation Induced Surface Compressive Stress for Preventing Dendrite Penetration in Solid-State Electrolytes

Xuhui Yao, Emilia Olsson, Manman Wang, Jianan Wang, Qiong Cai, Nianhua Peng,* *Roger Webb, and Yunlong Zhao**

Solid-state electrolytes (SSEs) have been thrust into the limelight for the revival of energy-dense lithium metal batteries, but still face the challenge of failure caused by the dendrite penetration. Mounting evidence indicates that dendrite penetration is related to the mechanical failure in SSEs, which calls for mechanical engineering to tackle this problem. This work reports a proof of concept that ion implantation induced surface compressive stress enables resistance in the dendrite penetration. A deterministic sequential multiple ion energies implantation is used to generate compressive stress, with implanted Xe ions distributed in a range of 160–600 Å from the surface. The symmetric lithium cells show that pellets with an implantation dose of 10^{13} Xe cm^{-2} exhibit stable stripping/plating cycles and extended lifespan, while a lower dose of 10^{12} Xe cm^{-2} cannot create sufficient stress to prevent dendrite penetration, and an excessive dose of 10^{14} Xe cm^{-2} leads to structural destruction and a decrease in stress. This improved performance is attributed to the induced surface compressive stress balanced over crystal grains, which is confirmed by grazing incidence diffraction techniques. The author's efforts demonstrate the usefulness of surface compressive stress to suppress dendrite penetration, offering more insight into rational stress–strain engineering as opposed to empirical optimization.

1. Introduction

The research in solid-state electrolytes (SSEs) dates back about 200 years to the study of ion migration in Ag_2S and PbF_2 by Michael Faraday, while the contemporary interest in SSEs for solid-state batteries emerged since the 1990s with the development of lithium phosphorus oxynitride by the Oak Ridge National Laboratory.[1,2] Over the past 10 years, the revival of lithium metal anode has been sweeping over the battery community. This interest was motivated initially by the high theoretical gravimetric and volumetric capacity of lithium metal anode and then built up to a climax with the development of SSEs.[3] The utilization of SSEs with high mechanical strength was thought to offer a feasible way toward rechargeable lithium metal batteries, tackling the safety concern caused by the flammable liquid organic electrolytes and the lithium filaments (so-called lithium dendrites) penetration.[4] By virtue of the

X. Yao, M. Wang, Y. Zhao
Advanced Technology Institute
University of Surrey
Guildford, Surrey GU2 7XH, UK
E-mail: yunlong.zhao@surrey.ac.uk
E. Olsson
Advanced Research Center for Nanolithography
Science Park 106, Amsterdam 1098 XG, Netherlands
E. Olsson
Institute of Physics and Institute for Theoretical Physics
University of Amsterdam
Postbus 94485, Amsterdam 1090 GL, Netherlands

The ORCID identification number(s) for the author(s) of this article can be found under https://doi.org/10.1002/smll.202108124.

E. Olsson, J. Wang, Q. Cai
Department of Chemical and Process Engineering
Faculty of Engineering and Physical Sciences
University of Surrey
Guildford GU2 7XH, UK
J. Wang
Department of Environmental Science and Engineering
State Key Laboratory of Multiphase Flow in Power Engineering
Xi'an Jiaotong University
Xi'an 710049, China
N. Peng, R. Webb
Surrey Ion Beam Centre
University of Surrey
Guildford GU2 7XH, UK
E-mail: n.peng@surrey.ac.uk
Y. Zhao
National Physical Laboratory
Teddington, Middlesex TW11 0LW, UK

**ADVANCED
SCIENCE NEWS**

www.advancedsciencenews.com

NANO · MICRO

small

www.small-journal.com

non-flammability, stacking batteries with SSEs and bipolar electrodes in a single package have attracted attention for large-scale applications, which also feature decreased system volume and increased energy density. The fundamental requirements for SSEs include high ionic conductivity and dielectric coefficient.[5–7] Previous efforts have led to significant development of SSEs with different chemistries, achieving comparable ionic conductivities (over 1 mS cm^{-1}) with conventional liquid electrolytes at room temperature.[8,9] Moreover, most SSEs are single-cation conductors, which generally possess higher transference numbers than liquid electrolytes.[10] Many comprehensive reviews have assessed the recent progress and summarized the fundamentals of SSE. Archer et al. has summarized failure modes and design concepts from SSEs' perspective.[11] Janek et al. has systematically assessed the physicochemical concepts of lithium metal anode in solid-state systems, including kinetic limitations and morphological stability.[12] Mukherjee et al. has also discussed the opportunity and demand for fast charging in practical applications.[13] Despite these achievements, more research efforts are required to improve further the dendrite resistance, structural stability, and interfacial stability of SSEs.

In SSEs research, the mechanical properties have received less attention compared to their electrochemical properties. Measuring the mechanical properties of SSEs and investigating the corresponding impacts are, however, critical for the application scenario of batteries. The mechanical properties include elasticity, plasticity, and fracture, which are generally determined from a stress–strain response curve. The elastic moduli of garnet-type $Li_{6.24}Al_{0.24}La_3Zr_2O_{11.98}$ were measured by Ni et al. using resonant ultrasound spectroscopy, revealing Young's modulus of 149.8 GPa, the shear modulus of 59.6 GPa and the bulk modulus of 102.8 GPa.[14] Yu et al. measured the elastic properties of garnet-type SSEs via nanoindentation, impulse excitation, and compared the values with the first-principle calculations.[15] Their results showed a good agreement between experiments and simulations and offered an essential reference for the development of SSEs. Generally, the kinetics and the electrochemical processes in SSEs are affected by various mechanical conditions. The degradation of SSEs and dendrite penetration are closely related to mechanical failure. For example, the internal compression within specific SSEs could hinder their ionic conductivities substantially; the SSEs with shear modulus over two times that of lithium metal might be able to prevent dendrite penetration.[16,17] Thereby, mechanical engineering is stepping into the spotlight and becoming a rising star to develop better SSEs. For example, Qi et al. argued that putting the SSEs surface into a condition of compressive stress could tackle the crack and dendrite issues of SSEs.[18] This perspective is theoretically valid, but experimental verification still needs to be performed to loop the circle of the proposition. It is no doubt that a robust understanding of mechanical conditions and corresponding effects on lithium metal battery performance could facilitate future breakthroughs of superior SSEs.

In this work, we first outline the fundamentals of stress in SSEs relevant to energy storage applications and examine the impacts of stress on lithium metal batteries and the approaches for placing stress in SSEs. Then, compressive stress is introduced deterministically at the surface of ceramic SSE pellets by ion implantation with different implantation doses and sequential multiple ion

energies. We investigate the relationship between the mechanical conditions and the electrochemical performance, with the focus on surface compressive stress and dendrite suppression.

2. Results and Discussion

For the common SSEs with polycrystalline structures and numerous grains, the stress is internal in the polycrystalline structure and balanced over grains in a wide range. The stress could arise from internal structural defects (such as atomic interstitials and vacancies) or external forces acting on the materials. To classify the different forms of stress in SSEs, an "unstressed" reference with determinate lattice parameters should be identified first (**Figure 1**a). When an SSE material is under stress, contractions and/or elongations are generated within the crystal lattice, which changes the inter-planar spacing (*d*-spacing) of the lattice planes. Usually, the tensile stress increases the *d*-spacing value (Figure 1b), with the converse being true for compressive stress (Figure 1c). These changes in *d*-spacing value can be reflected through a peak shift in the X-ray diffraction (XRD) pattern. By measuring the peak shift and the change in *d*-spacing value, the strain can be evaluated and, thus, the stress within the SSEs deduced.

The stress acting on a material includes the normal and shear stress. The definition of normal stress is stress acting normal (perpendicular) to the plane surface. For instance, the normal stresses (σ_x, σ_y, and σ_z) applied along the *x*, *y*, and *z*-direction and perpendicular to the plane surface are shown in Figure 1d, respectively. The positive values are conventionally used to denote tensile stress, and the compressive stress is denoted by the negative values. The definition of shear stress is that stress acting along the plane and perpendicular to the normal stress. The first denotation of the shear stress subscript indicates the plane where the shear stress is acting, and the second shows the direction of the shear stress. Any pure shear case can be converted to pure normal stress in a global coordinate system. For instance, the pure shear stress aligns with the red square axes, equivalent to the simple tension and compression acting to the blue square inscribed in the red square (Figure 1e). Therefore, for any stress condition in an SSE material, a specific 3D coordinate system can be defined, in which only tensile and compressive stress (namely principal stress) act. These principal stresses are denoted as σ_1, σ_2, and σ_3, and their corresponding directions are perpendicular to each other. The specification of the principal stress offers a feasible way to describe the stress condition in SSE materials.

The applied stress on SSEs could lead to impacts on their ionic conductivities. For most electrolytes, the ion transport follows the Nernst-Planck equation, but the convection term could be negligible.[11] Then the electrolyte conductivity can be simplified into the well-acknowledged Arrhenius equation (*E1*) (full derivation can be found in the reference):[11]

$$\sigma_i = \frac{\sigma_o}{T}\exp^{-\frac{E_a}{RT}} \tag{1}$$

The exponential prefactor (σ_o) is a weak function regarding temperature, and E_a represents the total activation energy for the
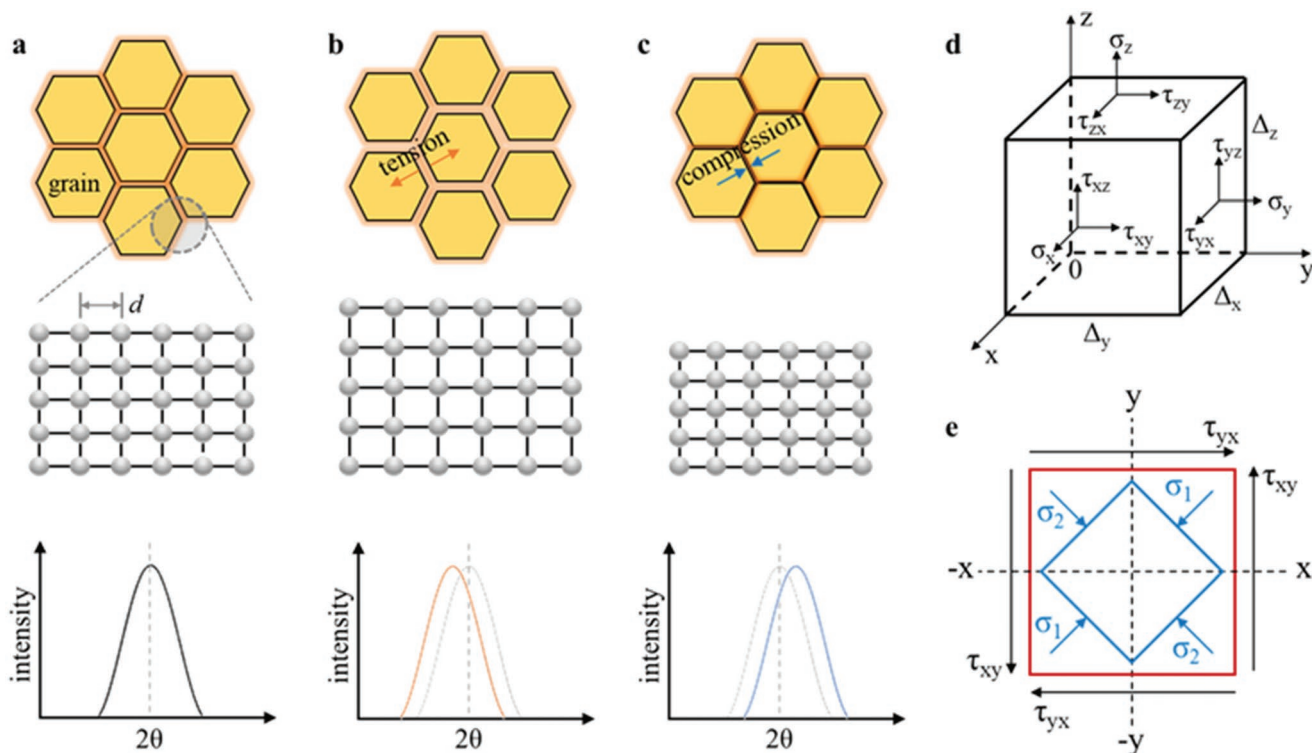
Figure 1. a–c) The top row gives representations of a) unstressed reference, b) tensile stress, and c) compressive stress. The middle row and the bottom row indicate the signatures of each stress states in lattice and diffraction patterns, respectively. d) Schematic diagram of stresses acting on an elemental unit. e) Sign convention for shear stresses and illustration of principal stress in a global coordinate system for a pure shear case.

formation of free ions and the migration of ions in the SSEs. Therefore, the ionic conductivity depends directly on the difficulty of the free ions formation and the energy barrier for their diffusion in the electrolyte. Most SSEs have periodic crystal structures with coordinated polyhedrons, which generally obey the Arrhenius equation (E1).[11] The lithium transport in SSEs is then well-acknowledged through the hopping within the bulk of the grains and the passway along grain boundaries. Theoretically, ions move from one energetically site to another favorable site by hopping after an infinitely long relaxation time. It is no doubt that the change in lattice parameters (d-spacing value) caused by the stress can impact the energy barrier for ion diffusion, leading to the change in ionic conductivity of SSEs.

To evaluate the impacts of stress on SSEs and its accompanying changes in lattice parameters on the ion transport kinetics, molecular dynamics (MD) simulations have been performed as specified in Experimental Section. The garnet-type $Li_{6.4}La_3Zr_{1.4}Ta_{0.6}O_{12}$ (LLZTO) is taken as an example because of its chemical stability and high ionic conductivity. To obtain the (self)diffusion coefficients of lithium (D_{Li}) in LLZTO, MD trajectories were simulated over 2 ns, with 0.5 ns equilibration time, at a different level of stress, whereby the mean square displacement (MSD) graphs were obtained (**Figure 2**a). The higher the D_{Li}, the more rapid the ionic conductivity (Equations (E5) and (E6) in Experimental Section). Simulating LLZTO at 300 K at different levels of stress (tensile stress of 10 Gpa and compressive stress of −10, −20, and −30 Gpa), a clear stress relationship with lithium diffusion was shown in Figure 2b. Increasing compressive stress leads to a slight decrease in D_{Li}, whereas a

corresponding increase in tensile stress leads to a more dramatic increase in D_{Li}. Comparing the changes in lattice parameter (Table S1, Supporting Information) with stress, it is clear that the increased lattice volume under tensile stress has a positive impact on the lithium-ion kinetics, with the larger lattice volume leading to more rapid lithium kinetics, in terms of D_{Li} (9.24×10^{-5} versus 3.890×10^{-4} Å^2 ps^{-1} going from 0 GPa to the tensile stress of 10 GPa). The fundamental behind the increase in D_{Li} is that expansions in lattice volume provide more space for lithium ions migration within the bulk of the grains and along grain boundaries. The compressive stress has a less dramatic effect on the lithium kinetics, with D_{Li} being largely constant between compressive stress 0 and 10 GPa. These results are in agreement with MD simulations of undoped $Li_7La_3Zr_2O_{12}$,[18] which concluded that with reduction of the cell volume (compressive stress), the available space for lithium mobility is also reduced, whereas the volume increase at low tensile stress opens up the lattice (see the increased value of a and c in Table S1, Supporting Information) enabling faster ionic conduction.

According to the theoretical linear elasticity model put forward by Monroe and Newman, electrolyte with high shear modulus could inhibit dendrite penetration.[19–22] However, in experimental cases, the lithium dendrite can still penetrate the high moduli SSEs, which even occurs readily.[23,24] The intrinsic defects in pellets and the cracks with (sub) micrometer size generated during battery cycling have been known as the main reasons. Once the cracks develop, the dendrite penetration is inevitable.[25] The propagation of dendrites, in turn, promotes
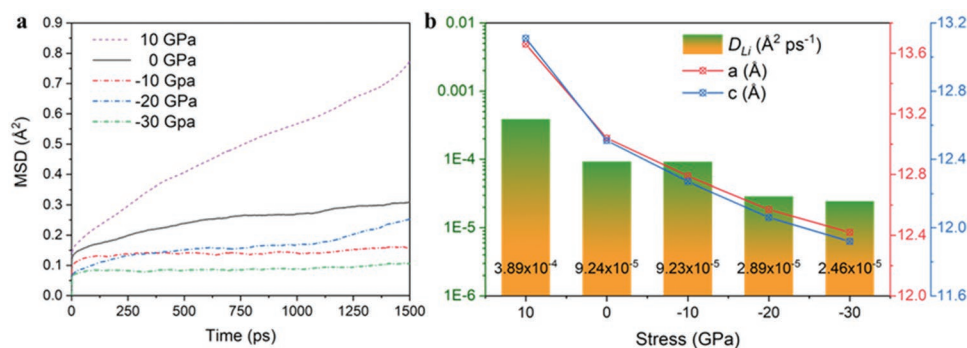
Figure 2. a) Mean square displacement (MSD) versus time for LLZTO at 300 K and b) lithium diffusion coefficients (D_{Li}), and lattice parameters a and c (b is equal to a) for LLZTO under tensile (10 GPa) stress, no stress (0 GPa), and compressive (−10, −20, and −30 GPa) stress.

mechanical fracture and cause the failure of SSEs. It may lead to a short circuit when the dendrites reach the cathode. Generally, the local tensile stress could result in highly brittle materials.[26] It is the common residual stress generated from machining, polishing or heterogeneity.[27–29] Based on the analogy to stress corrosion cracking that is commonly seen in the combined action of a chemical reaction and local tensile stress, the local tensile stress in SSEs can lead to the crack propagation and then promote lithium dendrite growth.[18] On the contrary, the compressive stress, if it is high enough, can force the cracks generated by the dendrite to close up.[18] Thereby, the compressive stress in SSEs could contribute to inhibiting dendrite propagation and penetration. Furthermore, plenty of evidence has pointed out that lithium dendrite could nucleate and propagate both on the surface and directly inside the SSEs. For the surface compressive stress cases, only the lithium dendrite growth on the surface can be restricted, whilst the lithium dendrite may also still generate directly inside the SSEs. But, one thing we believe for sure is that in this case, the lithium dendrite cannot be able to penetrate across the entire SSEs. In other words, the surface compressive stress can prevent the dendrite penetration across the SSEs rather than completely eliminate the dendrite formation inside the SSEs.

To introduce surface compressive stress, shot peening is the most widely used technique.[30] Through this cold-processing technique, a large number of small hard particles (such as metal, ceramic or glass) impinge on the surface of targets with sufficient acceleration energy to plastically deform the surface and put the surface into a compressive state. For the ceramic-type targets, some commercialized techniques, including laser shock peening (LSP), ion exchange, and ion implantation, have been developed. The LSP typically introduces shockwaves into the material via a laser-plasma confining medium. The protection (sacrificial) layer is often applied to avoid laser ablation. However, the LSP cannot create enough compressive stress (less than 1 GPa) for SSEs, and sometimes, it may even lead to the introduction of tensile stress.[18,31] The ion exchange typically introduces compressive stresses by exchanging small ions (alkali or alkali-earth ions) with larger ions, but only a few kinds of ions can be introduced. More importantly, monovalent ions, especially lithium ions, are much easier to be exchanged than others, which may lead to the reduction of ionic conductivity.[32,33] Ion implantation is also a cold-processing technique by which external ions are accelerated and implanted into the

targets, resulting in the alteration of targets' physical, chemical, mechanical or electrical properties.[34] The ion implantation features the advantage of orientationally tailoring the surface structure of the material (even the non-equilibrium states) by controlling the species and number of energetic implanted ions as well as the implantation depth (spatial distribution). It has been widely used to develop and strengthen many kinds of materials such as glasses, polymers, and ceramics for decades. For instance, it has been used to modify the electronic properties of semiconductors as well as to strengthen non-conducting ceramics.[18,35] So, the ion implantation modification for solid-state electrolytes could be realized with off-the-shelf implanters in the industry, including the micro battery through integrating semiconductor processing. To the best of our knowledge, neither the mechanical modification for SSEs via ion implantation nor the impacts on mechanical condition and electrochemical performance have been studied yet.

To introduce the compressive stress, Xe ions have been chosen and implanted on the surface of LLZTO pellets (**Figure 3**a). Here Xe is chosen because of its inertness and sizeable atomic radius. As a special advantage of charged particle radiation, the number of implanted ions (namely dose) can be monitored and controlled by the integral of beam current over time. To find the appropriate dose for introducing sufficient surface compressive stress into the LLZTO, several different peak Xe ion implantation levels have been explored. Specifically, the sample with a low peak implantation dose of 10^{12} Xe cm^{-2} is denoted as LLZTO-L (LLZTO-M for a medium dose of 10^{13} Xe cm^{-2} and LLZTO-H for a high dose of 10^{14} Xe cm^{-2}). Theoretically, the average depth of ion penetration is determined from the ion species, acceleration energy, and the composition of the target. Sequential multiple ion energies implantations have been implemented for each sample to achieve a uniform and broad depth of the Xe ion implantation layer. As shown in Figure 3b, the projected ranges for each acceleration energy and the overall weighted distribution have been simulated using Stopping and Range of Ions in Matter (SRIM) software based on the Monte Carlo simulation and the binary collision approximation.[36,37] The average ranges of 160, 310, 500, and 600 Å are obtained by the ion energies of 30, 80, 150, and 190 keV, respectively. The implanted Xe ion should mainly distribute within the range of 160–600 Å accordingly. The detailed results of the simulation are shown in the Supporting Information and Figure S1, Supporting Information. When an accelerated ion

ADVANCED
SCIENCE NEWS
www.advancedsciencenews.com

NANO · MICRO
small
www.small-journal.com
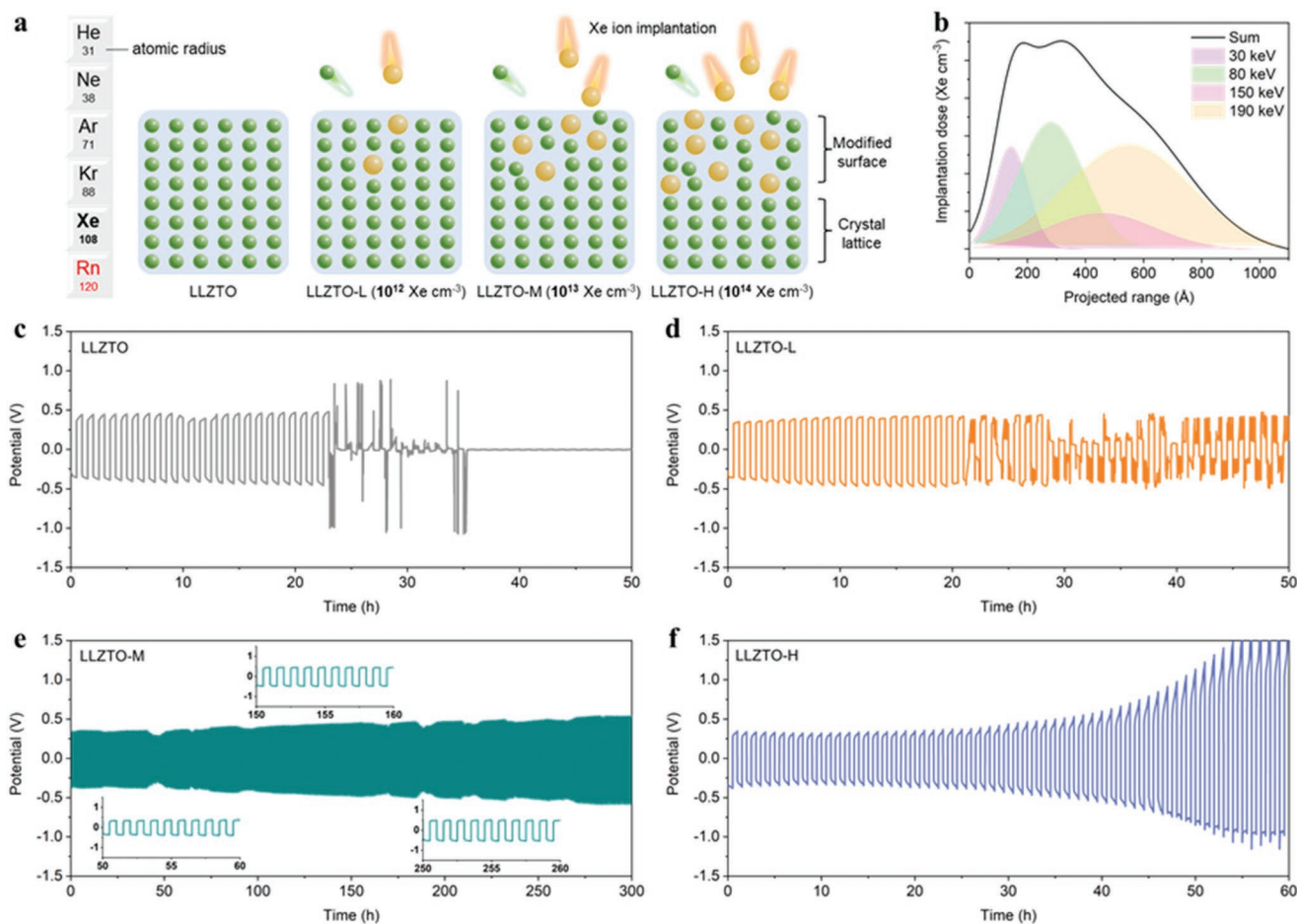
Figure 3. a) Schematic illustration of the Xe ion implantation and atomic radius table for noble gases. b) Projected range distribution for each accelerating voltage and overall weighted distribution for the Xe ion implantation. Galvanostatic cycling performance of the lithium plating/stripping in the symmetric lithium cells assembled with c) LLZTO, d) LLZTO-L, e) LLZTO-M, and f) LLZTO-H at room temperature (current density: $0.1 \ mA \ cm^{-2}$).

penetrates through the target, it ionizes atoms of the target and deposits damages along its path. The energy loss by the accelerated ion is inversely proportional to the square of its velocity, which means the major displacement caused by the projected ion locates just before the ion comes to a complete stop. Therefore, the distribution of the damages or the atomic displacement in this case is approximate to the depth distribution for the projected ions.

The electrochemical performance of the pristine LLZTO pellet and ion implanted samples have been evaluated by lithium plating/stripping in symmetric cells under a current density of $0.1 \ mA \ cm^{-2}$ at room temperature as specified in Experimental Section. The capacity has been fixed at $0.05 \ mAh \ cm^{-2}$ for each plating/stripping process. As shown in Figure 3c, the voltage profiles of the symmetric cells assembled with LLZTO pellets show an abrupt drop of the potential occurring just after 20 h of lithium plating/stripping cycling. The cells behave as a short-circuit state in subsequent cycles, that is, the potential remains close to 0 V. For the cells assembled with LLZTO-L pellets, the abrupt potential drop is still observed after 20 h cycling (Figure 3d). The difference is that the cells are not completely short-circuited but exhibit fluctuant potentials between normal and 0 V in subsequent cycles. It is worth

noting that no abrupt potential drop can be observed even after 300 h of cycles for the cells assembled with LLZTO-M pellets (Figure 3e). The zoom-in voltage profiles show stable lithium plating/stripping curves throughout the processes. For the cells assembled with LLZTO-H pellets, no potential drop has been observed after 60 h cycling, but the value of potential is continuously increasing to over 1 V (Figure 3f). A well-established term of critical current density (CCD, J^*) is used to describe the maximal current tolerance before the breakdown, which is closely related to dendrite penetration. To evaluate the CCD value, the galvanostatic stripping/plating experiment under increasing current densities is one of the most straightforward strategies. We have performed tests for pristine LLZTO and LLZTO-M samples to investigate the impacts of compressive stress on the CCD value (Figure S2, Supporting Information). The potential drop has been observed since $0.3 \ mA \ cm^{-2}$ for the cells assembled with LLZTO pellets, while the stable potential curves can be seen until $0.6 \ mA \ cm^{-2}$ for the LLZTO-M pellets. Given the above results, the impacts of different implantation doses on the electrochemical performance of LLZTO pellets are concluded as the following three points: I) The LLZTO and LLZTO-L samples show similar degradation behavior of short-circuit after 20 h cycling. II) The LLZTO-H samples show
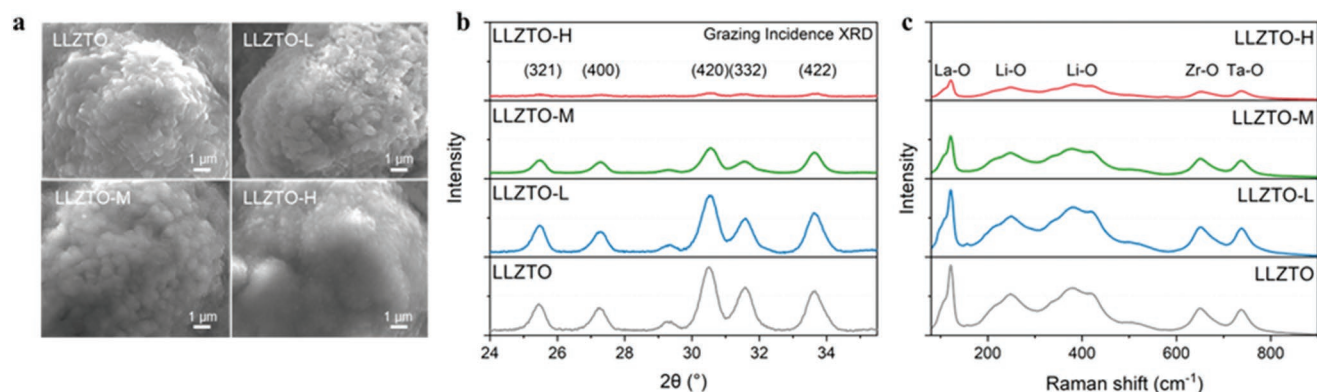
Figure 4. a) Surface morphologies, b) GI-XRD patterns, and c) Raman spectra of the LLZTO pellet and the pellets after the different doses of Xe ion implantation. All instrument parameters are the same for each sample, all pellet bodies come from the same preparation method, and all the patterns are drawn in the same scale.

extended lithium stripping/plating cycles but suffer from the increase of impedance. III) The LLZTO-M samples possess the ability to prevent short-circuit and to extend the lifespan of lithium metal batteries.

To investigate the reasons for the above different electrochemical performances, several surface characterizations have been performed to reveal structural variations created by different doses of ion implantation. From the scanning electron microscope images (**Figure 4**a), the surfaces of the LLZTO and LLZTO-L samples show plenty of sharp grains. Many smooth grains can be seen on the surface of LLZTO-M pellets. From the surface of LLZTO-H samples, no clear grains can be found, and the overall surface integrates into a smooth whole. These results indicate that energetic implanted ions can deform the surface morphology. The higher the implantation dose, the more the deformation in the surface. The pellets surfaces become more and more smooth with the dose increase. To investigate the lattice information from the surface, the grazing incidence X-ray diffraction (GI-XRD) characterization has been performed, which utilized a small incident angle to limit the X-ray beam penetrating the surface layer. Figure 4b shows the GI-XRD patterns for each sample, indicating that the intensities of diffraction peaks decrease with the increase of implantation dose. These peak intensities represent the crystallinity degree of the samples' surface, and to some extent, can reflect the levels of atomic displacement caused by ion implantation. Generally, crystalline materials yield intense peak intensities, while their amorphization counterparts show relatively broader and less intense peak intensities. The peak intensities obtained from the surface of LLZTO-L samples show similar intensities as the pristine LLZTO samples. Each peak can be indexed to a specific lattice plane of the cubic garnet phase, which is in good agreement with previous reports.[38] The LLZTO-M samples show relatively weaker peak intensities compared with the pristine LLZTO, which indicates that many atomic displacements have been created in the surface structure. Only some bumps can be seen from the GI-XRD patterns of LLZTO-H samples, indicating that the high implantation dose results in significant damages to the crystal structure of the surface. Raman scattering is another technique that is

sensitive to crystal structure. As shown in the Raman spectra for each sample in Figure 4c, each vibrational band can be assigned to LaO_8 dodecahedral unit, LiO_6 octahedral unit, LiO_4 tetrahedral unit, ZrO_6 octahedral unit, and TaO_6 octahedral unit, respectively, which is in good agreement with the previous reports.[39] Similar to the patterns of intensity in GI-XRD results, the Raman spectra obtained from the surface of LLZTO-M samples show relatively low intensities compared with pristine LLZTO and LLZTO-L samples, and the LLZTO-H samples show very weak intensities. These results reveal that the higher the implantation dose, the lower crystallinity and more atomic displacements. In the practice of ion implantation, the increasing atomic displacements generally result in the increase of compressive stress at the surface of the target.[40,41] Thereby, there would be no sufficient surface compressive stress for the LLZTO and LLZTO-L samples, and the improved lifespan of LLZTO-M and LLZTO-H samples could be attributed to the ion implantation induced surface compressive stress. However, excessive ion implantation dose above the amorphization threshold value could lead to glass transition or complete amorphization of the target material. Then the surface layer becomes ductile, and the induced compressive stress decreases dramatically after that because of the extension of the material.[42] On the other hand, the defects caused by ion implantation can migrate and cluster with each other, resulting in inter-connected defects or dislocation loops. In excessive cases, many defect clusters could peel off the surface material from the bulk phase, resulting in a contact loss at the surface. Garbayo et al. reported that the poly-amorphous phase would lead to many disconnected crystalline regions, which may increase the interfacial impedance of the batteries.[43] The significantly reduced crystallinity in LLZTO-H shows structural destruction, and many defects are possibly created. The ion diffusion during the electrochemical reaction might facilitate the migration of the defects and the formation of defect clusters. The defect clusters then lead to contact loss and increased local current density. Thereby, the increased overpotential in LLZTO-H is attributed to the structural destruction caused by excessive ion implantation dose.

To further measure the stress condition in different samples and investigate the cause of the improved cycling
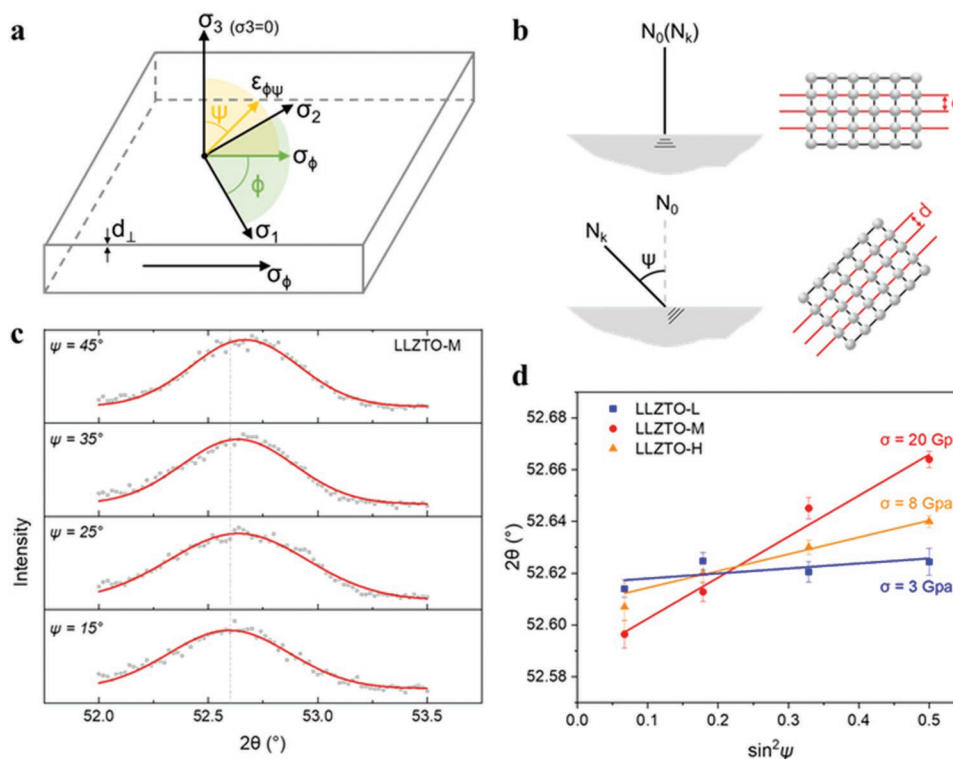
Figure 5. a) Schematic illustration of the general strain ($\varepsilon_{\varphi\psi}$), which is in response to the inter-surface stress (both σ_1 and σ_2) and perpendicular stress (σ_3) to the surface. The σ_φ represents the overall stress acting within the surface for the case of surface stress in an isotropic SSE. b) Schematic illustration of stress measurement. The diffraction plane is fixed, and the tilt angle ψ of the specimen is adjustable, where N_0 represents the normal (perpendicular) direction, and the angle of N_k shows the diffraction vector. c) GI-XRD spectra at different tilt angles for the LLZTO-M, with the measured points and the Gaussian fitted line. d) Residual strain distribution for different samples (diffraction data as a function of $sin^2\varphi$). The error bar is based on the standard deviation of the 2θ.

durability, the classical $sin^2\psi$ method together with GI-XRD measurements have been implemented. In evaluating stress, the strain (ε) in the crystal lattice is measured. It is the structural deformation in response to applied stress (σ) on the material. Then based on Hooke's law, the corresponding stress can be deduced from the material's elastic constants (E). This process is valid by assuming a linear elastic distortion of the appropriate crystal lattice plane. For the cases of surface stress in isotropic materials, there should only be stress (σ_φ) acting within the surface along an inclined line based on the Elasticity theory (**Figure 5**a). By combing Hooke's law, Poisson's ratio (ν), Young's double-slit experiments, Huygen's principle and Bragg's Law, the inter-plane stress (σ_φ) can be described as (All derivation can be found in the Supporting Information):

$$\sigma_\phi = \frac{E}{(1+\nu)sin^2\psi}\left(\frac{d_\psi - d_n}{d_n}\right) = -\frac{E}{2(1+\nu)}\frac{\pi}{180}\cot\theta_n\frac{\partial(2\theta)}{\partial sin^2\psi} \quad (2)$$

This equation allows us to calculate the stress based on the d-spacings obtained from two diffraction measurements. The measurements are made in a plane that is normal to the specimen surface and contains the diffraction vector (Figure 5b). Here we define:

$$C = -\frac{E}{2(1+\nu)}\frac{\pi}{180}\cot\theta_n \quad (3)$$

where C is a constant when the diffraction angle is determined, so, there is a linear function between $sin^2\psi$ and 2θ, which is shown as follows:

$$\sigma_\phi = C\frac{\partial(2\theta)}{\partial(sin^2\psi)} \quad (4)$$

Through several diffraction measurements achieved at different ψ tilts, the stress can then be obtained from the slop of $sin^2\psi$-2θ line. This method has been applied widely for probing stress in many materials, such as TiN and ZrO$_2$.[44–46] As shown in Figure 5c for LLZTO-M (LLZTO-L and LLZTO-H are shown in Figure S3, Supporting Information), the high 2θ angle belonging to the lattice plane (642) has been fixed, and a series of diffraction patterns have been obtained at gradient instrument tilt angle ψ from 15° to 45°. Choosing a high diffraction angle is because its high multiplicative factor can provide more reliable structure symmetry information. For each tilt angle, the diffraction data have been fitted via the Gaussian distribution function, and then the peak value has been generated. A systematic peak shift to a higher 2θ angle can be observed as the tilt angle increases, indicating that the (642) crystal planes show enlarging distance when turning to the out-of-plane angle. In addition, linear relationships between the $sin^2\psi$-2θ curve with positive slope values can be seen from the fit lines in Figure 5d.

ADVANCED
SCIENCE NEWS
www.advancedsciencenews.com

NANO · MICRO
small
www.small-journal.com

These results reveal that the surfaces of all samples are subjected to compressive stress because all slope values are positive. The approximate compressive stress value of 20 GPa for LLZTO-M (3 Gpa for LLZTO-L and 8 Gpa for LLZTO-H) can be deduced based on the slope values of the $\sin^2\psi$-2θ curves and Young's modulus of 150 GPa from the reference.[14,15] Thereby, based on the understanding that sufficient compressive stress can strengthen materials and resist stress corrosion cracking, it is believed that the extended lithium stripping/plating cycling lifespan of the LLZTO-M samples is attributed to the strong surface compressive stress. The lower dose cannot create sufficient compressive stress, and an excessive dose leads to a decrease in surface compressive stress.

3. Conclusion

In this work, the definition, measurement and impacts of stress in SSEs have been summarized systematically to guide rational mechanical engineering for developing SSEs in the application of lithium metal batteries. The appropriate compressive stress contributes to a durable SSE because it can resist lithium dendrite penetration through the SSE. As a proof of concept, the surface compressive stress has been introduced into the garnet-type LLZTO via sequential multiple ion energies implantation techniques with Xe ions. The appropriate implantation dose has been investigated, revealing that the LLZTO-M samples with the dose of 10^{13} Xe cm^{-2} exhibit improved durability of 300 h lithium stripping/plating cycles. The surface compressive stress in LLZTO-M samples has been confirmed via GI-XRD measurements and the $\sin^2\psi$ method. We believe mechanical engineering is a very attractive methodology that allows us to tackle dendrite issues and develop better SSEs. Furthermore, developing characterization technologies (such as X-ray computerized tomography and Time-of-Flight secondary ion mass spectrometry chemical mapping) to visualize dendrite growth behavior in SSEs can help to further understand the relationship between dendrite and stress. This will offer guidance for rational mechanical engineering for SSEs in the future.

4. Experimental Section

Implementation of Ion Implantation: The LLZTO pellet with a thickness of 1 mm and diameter of 14.3 mm was purchased from Limao New Material Co., Ltd. Ion implantation was carried out at Surrey Ion Beam Centre (UK) using the Danfysik 1090 implanter. Xe ions were chosen to avoid possible chemical effects from the implanted ions. The samples were implanted with Xe ions of 190, 150, 80, and 50 keV to create a flat damage profile and uniform distribution of Xe. Projected ranges were calculated using the Stopping and Range of Ions in Matter (SRIM) software with the core program of Transport of Ions in Matter (TRIM). Target density was set to 4.60 g cm^{-3}, which equals 7.2989×10^{22} atoms cm^{-3}.

Structural, Electrochemical, and Mechanical Measurement: The surface morphologies were captured using field-emission scanning electron microscopy (FE-SEM, JEOL JSM-7100F). Structural Information was characterized by an X-ray diffractometer (PANalytical X'Pert Pro) and a Raman spectrometer (Renishaw Microraman). Stress analysis was performed through a Bruker Discover D8 diffractometer. The symmetric lithium cell was prepared in an Ar-filled glove box. To assemble symmetric lithium cells, the lithium plates and the LLZTO pellet were used as electrodes and the electrolyte, respectively. The lithium plates with a diameter of 10 mm were used as purchased (Tob New Energy Technology Co., Ltd.). Two lithium plates were attached on both sides of the LLZTO pellet between two stainless mesh and heated to 170 °C via a hot plate. The sandwich-like battery was then put into a CR2032 coin cell case, and the cell was heated to 200 °C to realize a conformal interface contact.[47] The cell was cooled down to room temperature for electrochemical testing. The galvanostatic cycling performance was tested via a battery testing system (CT-4008-5V10mA, Neware Technology Ltd.). The cell clips were used to provide gentle pressure to ensure continuous good contact.

Molecular Dynamics Simulations: All MD simulations were conducted in the DL_POLY 4.10 code.[48,49] The Ta-doped systems were constructed by doping a $Li_{56}La_{24}Zr_{16}O_{96}$ cell from Materials Project.[50] Using atomsk, a $2 \times 2 \times 2$ supercell containing 2304 atoms was then generated and equilibrated at 300 K during an NPT run (constant number of atoms, pressure, and temperature).[51] For all simulations, the timestep was 0.1 fs. For the simulations, the Buckingham potential with shell model from Wang et al.[52] was used. For the compressive and tensile stress simulations, the lattice vector of the simulation cells was varied from 12.42 to 13.66 Å to capture the appropriate stress. These simulation cells were then run for 2 ns NVT (constant number of atoms, volume, and temperature) with 0.5 ns of the trajectory being equilibrated. From the MSD, D_{Li} in the different systems were then obtained according to:[53]

$$r^2(t) = 6D_{Li}t + B_{Li} \tag{5}$$

In the above equation, $<r^2(t)>$ is the time-dependent MSD, t represents time, and B_{Li} is a thermal factor associated with atomic vibrations. D_{Li} is related to the ionic conductivity (σ_{Li}) through the following equation, showing that a higher D_{Li} also indicates a higher ionic conductivity.[54]

$$\sigma_{Li} = \frac{C_{Li}q^2D_{Li}}{k_BT} \tag{6}$$

C_{Li} is lithium concentration, q is the lithium ionic charge, k_B is Boltzmann's constant, and T is temperature.

Supporting Information

Supporting Information is available from the Wiley Online Library or from the author.

Conflict of Interest

The authors declare no conflict of interest.

Data Availability Statement

The data that support the findings of this study are available from the corresponding author upon reasonable request.

Keywords

[1] P. G. Bruce, *Solid State Electrochemistry*, Cambridge University Press, Cambridge **1997**.

[2] J. Bates, N. Dudney, G. Gruzalski, R. Zuhr, A. Choudhury, C. Luck, J. Robertson, *Solid State Ionics* **1992**, *53*, 647.

[3] D. Lin, Y. Liu, Y. Cui, *Nat. Nanotechnol.* **2017**, *12*, 194.

[4] R. Sakanoi, T. Shimazaki, J. Xu, Y. Higuchi, N. Ozawa, K. Sato, T. Hashida, M. Kubo, *J. Chem. Phys.* **2014**, *140*, 121102.

[5] J. B. Goodenough, Y. Kim, *Chem. Mater.* **2010**, *22*, 587.

[6] L. J. Miara, S. P. Ong, Y. Mo, W. D. Richards, Y. Park, J.-M. Lee, H. S. Lee, G. Ceder, *Chem. Mater.* **2013**, *25*, 3048.

[7] A. Manthiram, X. Yu, S. Wang, *Nat. Rev. Mater.* **2017**, *2*, 16103.

[8] N. Kamaya, K. Homma, Y. Yamakawa, M. Hirayama, R. Kanno, M. Yonemura, T. Kamiyama, Y. Kato, S. Hama, K. Kawamoto, *Nat. Mater.* **2011**, *10*, 682.

[9] R. Murugan, V. Thangadurai, W. Weppner, *Angew. Chem., Int. Ed.* **2007**, *46*, 7778.

[10] J. C. Bachman, S. Muy, A. Grimaud, H.-H. Chang, N. Pour, S. F. Lux, O. Paschos, F. Maglia, S. Lupart, P. Lamp, *Chem. Rev.* **2016**, *116*, 140.

[11] Q. Zhao, S. Stalin, C.-Z. Zhao, L. A. Archer, *Nat. Rev. Mater.* **2020**, *5*, 229.

[12] T. Krauskopf, F. H. Richter, W. G. Zeier, J. r. Janek, *Chem. Rev.* **2020**, *120*, 7745.

[13] B. S. Vishnugopi, E. Kazyak, J. A. Lewis, J. Nanda, M. T. McDowell, N. P. Dasgupta, P. P. Mukherjee, *ACS Energy Lett.* **2021**, *6*, 3734.

[14] J. E. Ni, E. D. Case, J. S. Sakamoto, E. Rangasamy, J. B. Wolfenstine, *J. Mater. Sci.* **2012**, *47*, 7978.

[15] S. Yu, R. D. Schmidt, R. Garcia-Mendez, E. Herbert, N. J. Dudney, J. B. Wolfenstine, J. Sakamoto, D. J. Siegel, *Chem. Mater.* **2016**, *28*, 197.

[16] J. Pan, Q. Zhang, J. Li, M. J. Beck, X. Xiao, Y.-T. Cheng, *Nano Energy* **2015**, *13*, 192.

[17] A. Fluri, D. Pergolesi, V. Roddatis, A. Wokaun, T. Lippert, *Nat. Commun.* **2016**, *7*, 10692.

[18] Y. Qi, C. Ban, S. J. Harris, *Joule* **2020**, *4*, 2599.

[19] F. Shen, M. B. Dixit, X. Xiao, K. B. Hatzell, *ACS Energy Lett.* **2018**, *3*, 1056.

[20] M. D. Tikekar, S. Choudhury, Z. Tu, L. A. Archer, *Nat. Energy* **2016**, *1*, 16114.

[21] C. Monroe, J. Newman, *J. Electrochem. Soc.* **2003**, *150*, A1377.

[22] C. Monroe, J. Newman, *J. Electrochem. Soc.* **2005**, *152*, A396.

[23] Y. Ren, Y. Shen, Y. Lin, C.-W. Nan, *Electrochem. Commun.* **2015**, *57*, 27.

[24] E. J. Cheng, A. Sharafi, J. Sakamoto, *Electrochim. Acta* **2017**, *223*, 85.

[25] L. Ye, X. Li, *Nature* **2021**, *593*, 218.

[26] R. Garcia-Mendez, J. G. Smith, J. C. Neuefeind, D. J. Siegel, J. Sakamoto, *Adv. Energy Mater.* **2020**, *10*, 2000335.

[27] S. Trail, P. Bowen, *Mater. Sci. Eng., A* **1995**, *192*, 427.

[28] D. Liu, Y. Shi, X. Lin, C. Xian, *Int. J. Adv. Manuf. Technol.* **2019**, *100*, 1491.

[29] D. Wu, H. Wang, K. Zhang, X. Lin, *Int. J. Adv. Manuf. Technol.* **2019**, *103*, 2495.

[30] H. Kumar, S. Singh, P. Kumar, *Int. J. Eng. Sci. Emerging Technol.* **2013**, *5*, 12.

[31] R. Sundar, P. Ganesh, R. K. Gupta, G. Ragvendra, B. Pant, V. Kain, K. Ranganathan, R. Kaul, K. Bindra, *Lasers Manuf. Mater. Process.* **2019**, *6*, 85.

[32] L. Zhang, X. Guo, *J. Am. Ceram. Soc.* **2020**, *103*, 3971.

[33] X. Li, M. Meng, D. Li, R. Wei, L. He, S. Zhang, *J. Eur. Ceram. Soc.* **2020**, *40*, 4635.

[34] M. Liu, C. Li, L. Liu, Y. Ye, D. Dastan, H. Garmestani, *Mater. Sci. Technol.* **2020**, *36*, 284.

[35] A. Armini, S. Bunker, M. I. n Spitzer, in *16th Photovoltaic Specialists Conference*, IEEE, Piscataway, NJ **1982**, p. 895.

[36] J. P. Biersack, L. Haggmark, *Nucl. Instrum. Methods* **1980**, *174*, 257.

[37] J. F. Ziegler, J. P. Biersack, in *Treatise on Heavy-Ion Science*, Springer, New York **1985**, pp. 93–129.

[38] W. Li, C. Sun, J. Jin, Y. Li, C. Chen, Z. Wen, *J. Mater. Chem. A* **2019**, *7*, 27304.

[39] Y. Meesala, Y.-K. Liao, A. Jena, N.-H. Yang, W. K. Pang, S.-F. Hu, H. Chang, C.-E. Liu, S.-C. Liao, J.-M. Chen, *J. Mater. Chem. A* **2019**, *7*, 8589.

[40] Y. Jia, Z. Ba, X. Chen, B. Zhou, W. Zhou, H. Liu, Q. Dong, *Surf. Topogr. Metrol. Prop.* **2020**, *8*, 025015.

[41] C. Yan, Q. Zeng, W. He, J. Zhu, *Tribol. Int.* **2021**, *155*, 106816.

[42] R. A. Khmelnitsky, V. A. Dravin, A. A. Tal, E. V. Zavedeev, A. A. Khomich, A. V. Khomich, A. A. Alekseev, S. A. Terentiev, *J. Mater. Res.* **2015**, *30*, 1583.

[43] I. Garbayo, M. Struzik, W. J. Bowman, R. Pfenninger, E. Stilp, J. L. Rupp, *Adv. Energy Mater.* **2018**, *8*, 1702265.

[44] Z. Chen, N. Prud'homme, B. Wang, V. Ji, *Surf. Coat. Technol.* **2011**, *206*, 405.

[45] M. Stefenelli, J. Todt, A. Riedl, W. Ecker, T. Müller, R. Daniel, M. Burghammer, J. Keckes, *J. Appl. Crystallogr.* **2013**, *46*, 1378.

[46] A. Benediktovitch, T. Ulyanenkova, J. Keckes, A. Ulyanenkov, in *Advanced Materials Research*, Trans Tech Publications, Switzerland **2014**, pp. 162.

[47] K. K. Fu, Y. Gong, B. Liu, Y. Zhu, S. Xu, Y. Yao, W. Luo, C. Wang, S. D. Lacey, J. Dai, *Sci. Adv.* **2017**, *3*, e1601659.

[48] I. T. Todorov, W. Smith, K. Trachenko, M. T. Dove, *J. Mater. Chem.* **2006**, *16*, 1911.

[49] I. Bush, I. Todorov, W. Smith, *Comput. Phys. Commun.* **2006**, *175*, 323.

[50] A. Jain, S. P. Ong, G. Hautier, W. Chen, W. D. Richards, S. Dacek, S. Cholia, D. Gunter, D. Skinner, G. Ceder, *APL Mater.* **2013**, *1*, 011002.

[51] P. Hirel, *Comput. Phys. Commun.* **2015**, *197*, 212.

[52] Y. Wang, A. Huq, W. Lai, *Solid State Ionics* **2014**, *255*, 39.

[53] E. Olsson, J. Cottom, X. Aparicio-Anglès, N. H. de Leeuw, *Phys. Chem. Chem. Phys.* **2020**, *22*, 692.

[54] T. C. Yeh, J. L. Routbort, T. O. Mason, *Solid State Ionics* **2013**, *232*, 138.